Comparative Study of Quasi-random Sampling for Brain Tumor Segmentation in MRI Using Expectation-Maximization (EM) and Region Growing

Boucenna Sidahmed [1,*], Z. Chama [1], N. Taleb [2], B. Hachemi [3], and E. B. Bourennane [4]

[1] Electronics Photonics and Optronics Laboratory, Djillali Liabes University, Sidi Bel Abbes, Algeria
[2] Communication networks, architecture and multimedia, Djillali Liabes University, Sidi Bel Abbes, Algeria
[3] Center for the Development of Advanced Technologies (CDTA), Algiers, Algeria
[4] Imaging and Artificial Vision, University of Borgogne, Dijon, France
Email: sidahmed.boucenna@univ-sba.dz (B.S.); zouaoui.chama@univ-sba.dz (Z.C.); ne_taleb@univ-sba.dz (N.T.); b.hachemi@cdta.dz (B.H.); El-Bay.Bourennane@u-bourgogne.fr (E.B.B.)
*Corresponding author

***Abstract*—Brain tumor detection remains a challenging problem due to the complexity of tumor structures and variability in Magnetic Resonance Imaging (MRI) data. Accurate detection and segmentation of brain tumors in medical imaging are essential for effective diagnosis and treatment planning. This study presents a multi-segmentation approach for brain tumor localization combining the Expectation-Maximization (EM) algorithm with an improved region-growing classification technique. To improve segmentation accuracy and computational efficiency, several quasi-random sampling methods were evaluated, including Halton, Sobol, Hammersley, Faure, and Poisson Disk Sampling. Experimental results demonstrate that the Sobol sampling method achieves superior precision in delineating tumor and edema regions. Its robustness and efficiency make it particularly suitable for complex medical imaging applications. Although other sampling techniques also produced promising results, Sobol consistently outperforms them in both speed and accuracy. In conclusion, the study highlights the importance of adapting segmentation strategies to the dataset characteristics, clinical requirements, and operator expertise to ensure optimal performance in real-world implementation.**

***Keywords*—brain tumor segmentation, quasi-random sampling, sobol sequence, Magnetic Resonance Imaging (MRI), expectation-maximization, region-growing**

I. Introduction

Brain tumors present a significant public health challenge, making it essential to develop accurate and efficient detection methods. Magnetic Resonance Imaging (MRI) serves as a powerful modality for visualizing brain structures and pathological processes, offering detailed images crucial for accurate diagnosis [1]. However, detecting brain tumors remains inherently challenging, which has led researchers to adopt various robust and reliable classification techniques [2, 3]. This study focuses on comparing quasi-random sampling sequences, also known as low-discrepancy sequences, used within the region-growing classification technique for tumor tracing on MRI images (Fig. 1) [1, 3]. The paper explores the multi-classification of MRI medical images, which can be significantly enhanced by combining the Expectation-Maximization (EM) algorithm with region-growing refinement initialized via quasi-random sequences such as Halton, Sobol, Hammersley and Faure. In this hybrid approach, a low-discrepancy sequence (e.g., Halton or Sobol) generates uniformly distributed seed points in the intensity or spatial domain, ensuring that the EM clustering process starts from representative and evenly spread initial centroids. The EM algorithm then iteratively estimates class parameters and pixel membership probabilities, producing a coarse segmentation map. To improve boundary accuracy and suppress noise-induced misclassifications, region-growing is subsequently applied: starting from the high-confidence pixels identified by EM, connected regions expand based on local intensity similarity. Quasi-random sequences like Hammersley or Faure help reduce initialization bias, leading to more consistent multi-tissue classifications across successive runs. This synergy of statistical mixture modeling, structured sampling, and spatial refinement produces robust and high-precision segmentations of brain tissues and lesions in MRI. The quasi-random sequence (Halton, Sobol, Hammersley or Faure) is used to place the initial seeds for the region-growing stage instead of initializing the EM algorithm. After EM produces a soft classification map

Manuscript received March 3, 2025; revised March 27, 2025; accepted November 13, 2025; published July 16, 2026.

and identifies high-confidence pixels for each tissue class, a small subset is selected of those pixels according to the low-discrepancy sequence. This structured sampling avoids clustering of seed points that can occur with purely random sampling, ensures each that each anatomical region is covered by a representative growth front, and leads to more balanced, noise-robust boundary refinement, ultimately enhancing the precision and repeatability of the final multi-tissue MRI segmentation.

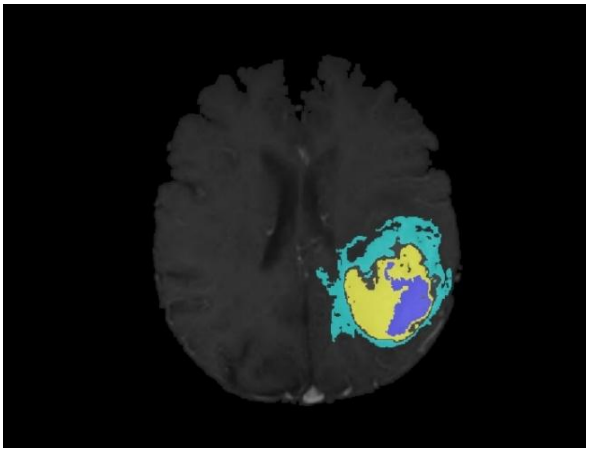

Fig. 1. Brain tumor detection.

Quasi-random sampling techniques such as Halton, Sobol, Hammersley, Faure, and Poisson Disk Sampling are designed to systematically distribute points across the image space, thereby improving region classification accuracy in MRI segmentation [4, 5]. This study further investigates the impact of these sampling methods on key evaluation metrics, including Hausdorff Distance (HD) and Average Distance (AVD), which are essential for assessing the precision and effectiveness of tumor segmentation [6, 7]. This investigation is motivated by the advantages of quasi-random sampling techniques over traditional approaches, which are often characterized by lower accuracy and higher computational costs [8]. By providing more uniform coverage, quasi-random sequences achieve greater accuracy and more reliable segmentation and classification results [4, 5]. The primary objective of this research is to advance tumor detection methodologies by evaluating the performance of quasi-random sampling methods against expert radiologist annotations, highlighting both the strengths and limitations of each approach. To further enhance segmentation performance, this study combines the Expectation-Maximization (EM) algorithm with quasi-random sampling within a region-growing classification framework, targeting early tumor detection in MRI systems [6]. This methodological advancement holds strong potential for oncology by improving imaging technologies used in tumor identification [7]. The comparative analysis evaluates the impact of various quasi-random sampling techniques on key performance metrics such as error rate, sensitivity, and specificity in tumor detection, providing valuable insights for healthcare professionals, researchers, and imaging specialists regarding on the benefits of integrating quasi-random sampling into MRI-based brain tumor segmentation workflows [8].

II. Description of Point Sequences

This study investigates the use of five quasi-random point sequences: Halton, Sobol, Hammersley, Faure, and Poisson Disk Sampling to evaluate their ability to generate low-discrepancy distributions that provide more uniform coverage of the spatial domain compared to purely random methods. This uniformity is essential for medical image segmentation, where the precision of point placement directly affects the precision of tumor delineation. The selection of these sequences was based on their theoretical strengths, as each offers distinct advantages for enhancing the robustness and reliability of brain tumor detection in Magnetic Resonance Imaging (MRI) data.

A. Halton Sequence

Generation Principle: The Halton sequence is constructed by using a distinct prime number as the base for each dimension. Specifically, the *i-th* dimension utilizes the *i-th* prime number as its radix. For a given index n, the corresponding value in the sequence is obtained by expressing n in the chosen prime base, reversing its digits, and interpreting the result as a fractional value [9]. The generation process can be mathematically expressed as shown in Eq. (1).

$$x_n = \sum_{k=0}^{\infty} \frac{d_k}{b^{k+1}} \quad (1)$$

The *n-th* number in the sequence is generated by reversing the digits of n in the corresponding base b, where d_k are the digits of n in the base b [10].

Characteristics: The Halton sequence is known for its simple algorithmic structure and low computational cost, which enable fast generation [11]. However, its deterministic construction makes it prone to interdimensional correlations, particularly in higher-dimensional spaces, which may affect the uniformity of its spatial distribution [12, 13].

Reason for Choice: The choice of the Halton sequence is motivated by its practical efficiency and suitability for lowdimensional sampling tasks, where it offers satisfactory uniform coverage [10]. Its ease of implementation and responsiveness to initial exploratory analyses make it a compelling candidate for early-phase segmentation experiments in medical imaging [9, 11].

B. Sobol Sequence

Generation Principle: The Sobol sequence is constructed recursively using direction numbers and binary representations, allowing the generation of points with low discrepancy properties [14]. Its formulation relies on base-2 digital construction methods that ensure uniform coverage of the unit hypercube, particularly effective in higher-dimensional spaces. The mathematical generation of each point in the sequence can be expressed as shown in Eq. (2).

$$\oplus^{\infty}{}_{k=0} a_k v_k \quad (2)$$

Characteristics: The Sobol sequence is renowned for its excellent low-discrepancy properties and computational efficiency, which makes it particularly well suited for high dimensional sampling and numerical integration tasks [15, 16]. Its construction ensures uniform coverage even in complex multidimensional domains.

Reason for Choice: The Sobol sequence was chosen for its ability to maintain uniformity in high-dimensional spaces, a property that is essential for robust and precise delineation in medical image segmentation [17]. This uniform sampling contributes to improved accuracy in the detection of tumor and edema regions, enhancing the overall performance of the segmentation process.

C. Hammersley Sequence

Generation principle: The Hammersley sequence in d dimensions uses the sequence numbers themselves for the first dimension and the Halton sequences for the other dimensions [18]. The mathematical formulation of the Hammersley sequence is expressed in Eq. (3).

$$x_n = \left(\frac{n}{N}, \Phi_{b_1}(n)\ \Phi_{b_2}(n) \ldots \Phi_{b_{d-1}}(n)\right) \quad (3)$$

where N is the total number of points, an $\Phi_b(n)$ is the radical inverse function in base b [19].

Characteristics: The Hammersley sequence is recognized for its excellent uniformity in low-dimensional spaces due to its deterministic structure and integration of the Halton sequence components [20]. Its low discrepancy nature makes it particularly advantageous for applications requiring precise spatial coverage in reduced dimensions.

Reason for Choice: The Hammersley sequence was selected for its ability to generate highly uniform point distributions in low-dimensional settings, which is particularly relevant for medical image segmentation tasks where spatial coherence is critical and dimensionality remains moderate [21, 22].

D. Faure Sequence

Generation principle: The Faure sequence extends the construction of the Halton sequence by employing a common prime base across all dimensions, combined with a systematic permutation of the digit coefficients in their base-b representations [23]. This refinement aims to reduce inter-dimensional correlations and enhance uniformity, particularly in moderate to high-dimensional spaces. The mathematical formulation of the Faure sequence is expressed in Eq. (4).

$$x_j(n) = \sum_{k=0}^{\infty} \frac{\sigma_j(d_k)}{b^{k+1}} \quad (4)$$

where $\sigma_j$is a permutation of the digits in base b.

Characteristics: The Faure sequence is designed to preserve low-discrepancy properties even as dimensionality increases, offering improved uniformity over the Halton sequence in various computational settings [24]. Its structural enhancements make it particularly suitable for complex sampling tasks where inter-dimensional correlations must be minimized.

Reason for Choice: The Faure sequence was chosen for its ability to maintain uniformly distribution points in higher dimensional spaces, a property that aligns with the requirements of advanced medical image segmentation tasks [25]. Its theoretical robustness in managing multidimensional variability contributes to more stable and reliable segmentation outcomes.

E. Poisson Disk Sampling

Generation principle: Poisson Disk Sampling generates a set of points that are randomly distributed while enforcing a minimum distance constraint between any two points, thereby avoiding clustering and promoting spatial uniformity. Typically implemented using the Bridson algorithm [26], the process starts with a randomly selected seed point and iteratively proposes new candidates within a predefined annular region. Each candidate is accepted only if it satisfies the minimum distance criterion relative to all previously accepted points, resulting in a distribution characterized by blue noise properties that are particularly well suited for image analysis tasks.

Algorithm: The steps of the Poisson Disk Sampling method are summarized below:

- Choose an initial random point in the domain.
- For each point, generate new candidate points within a radius range.
- Accept points that are farther than the minimum distance from existing points.
- Repeat until no more points can be added.

Characteristics: Poisson Disk Sampling is renowned for its ability to generate point distributions that are both spatially uniform and non-clustering due to the enforced minimum distance between samples. This spatial regularity leads to blue noise characteristics, which are particularly advantageous in applications requiring homogeneous coverage, such as medical image segmentation, where sampling consistency directly influences analytical precision.

Reason for Choice: Poisson Disk Sampling was selected for its ability to produce well-spaced point sets with reduced local density variations, thereby minimizing sampling bias and improving the reliability of region-based segmentation in MRI data [27]. Its intrinsic balance between randomness and regularity makes it a compelling choice for tasks that demand both spatial uniformity and anatomical fidelity. These point sequences offer unique advantages and characteristics that make them suitable for different aspects of image segmentation and classification. Their selection aims to improve the precision and effectiveness of tumor detection and segmentation in MRI images.

III. Image Preprocessing

The image preprocessing stage is crucial for preparing the MRI data for subsequent analysis. The sequence of steps involved in this process is illustrated in Fig. 2. The initial phase of the image preprocessing pipeline is marked by the importation of the MRI scan (Fig. 3) [28] into the MATLAB processing environment, followed by a verification step. This stage is essential not only for the

validation of data integrity but also to ensure that the input image aligns with the predefined analytical parameters. This validation process helps detect inconsistencies, anomalies, or artifacts that could compromise later stages of analysis, thereby reinforcing the robustness of the overall framework.

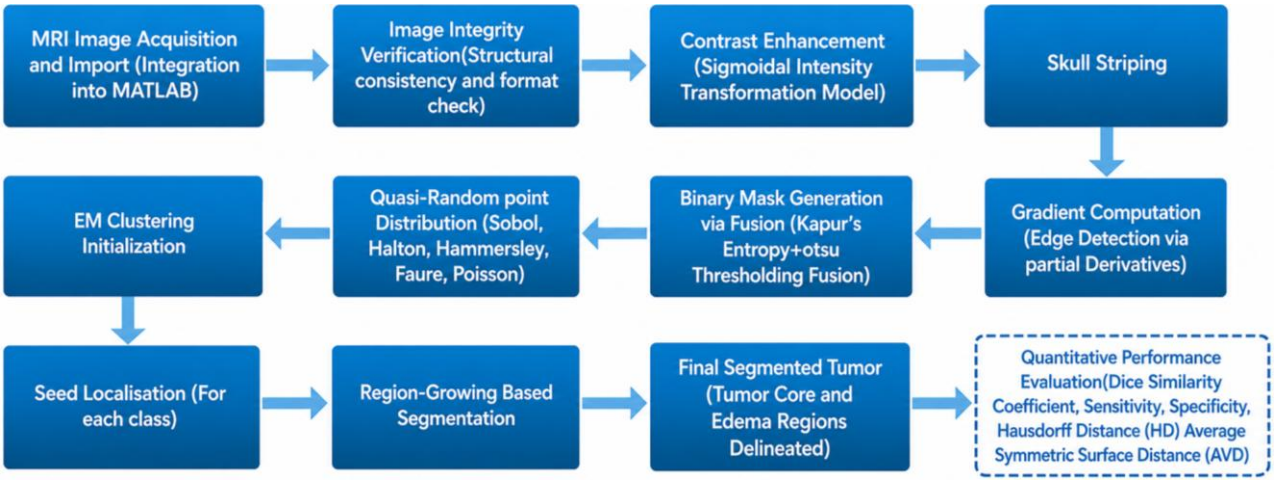

Fig. 2. Overview flowchart of the magnetic resonance imaging images preprocessing.

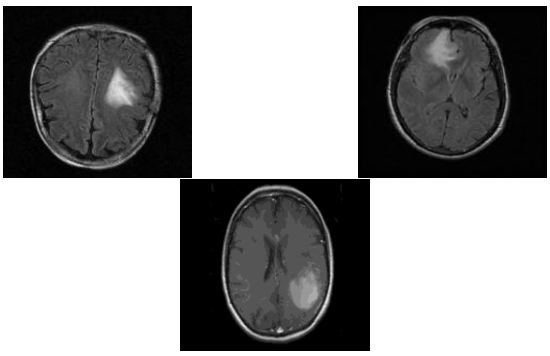

Fig. 3. Comparative visualization of three brain tumor types in MRI imaging.

In this study, a contrast adjustment (Fig. 4) was applied as a key preprocessing technique to improve the discernibility and resolution of the features of the image. This process was integrated to strengthen the efficacy of subsequent analytical procedures, thus facilitating the precise extraction of clinically relevant information. The contrast enhancement used a sigmoidal transformation, a nonlinear intensity mapping function renowned for its ability to effectively modify the image's intensity distribution. This transformation accentuates both subtle and high-contrast pixel variations. The mathematical formulation of the transformation is represented as follows:

$$I_{new} = \frac{1}{1+\exp(gain.(cutoff-1))} \quad (5)$$

where:

- I_{new} is the adjusted intensity value.
- I is the original intensity value of a pixel.
- gain controls the contrast adjustment; higher values increase the contrast.
- cutoff represents the midpoint of the intensity scale around which the contrast is adjusted.

Parameters gain and cutoff were selected according to their impact on image contrast:

- Gain: Determines the degree of contrast enhancement. For example, a gain value of 5 provides a neutral adjustment, while a value of 10 significantly increases contrast.
- Cutoff: Defines the point on the grayscale where the contrast is adjusted. A typical value is 0.5, which corresponds to the midpoint of the grayscale, though this may vary depending on specific image requirements.

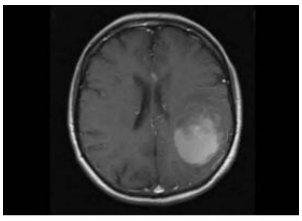

Before Adjusting Contrast

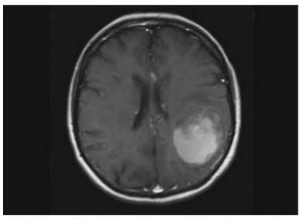

After Adjusting Contrast

Fig. 4. MRI image before and after adjusting contrast.

Using this sigmoidal transformation, the contrast between lighter and darker regions within the image was significantly accentuated. This process enhanced subtle intensity variations and produced clearer visual representations. The resulting improvement in image clarity plays a key role in refining the performance of subsequent processing stages, particularly for segmentation and feature extraction tasks, by enabling

more accurate delineation and identification of critical structures [29].

A. Skull Stripping

Before skull stripping, contrast enhancement was applied to the input MRI image using a sigmoid-based filter. This method emphasizes high-frequency regions and improves the visibility of fine anatomical details within the brain [30]. The sigmoid transformation modifies the gray-level distribution, to reduce similarities between adjacent regions, which is essential for enhancing structural contrasts. The gray level of the enhanced image I_{out} is calculated as follows:

$$I_{out} = \left(\frac{I_{max} - I_{min}}{1 + e^{-\alpha(I_{in} - \beta)}}\right) + I_{min} \quad (6)$$

where I_{in} represents the gray level of the input image, I_{max} and I_{min} denote the maximum and minimum gray levels of the output image, respectively, and α and β control the intensity range width and the center of the intensity range [31]. After the contrast enhancement, skull stripping was performed on the enhanced image to accurately extract brain tissue (Fig. 5). The Otsu's thresholding algorithm was used to identify an optimal threshold by minimizing intraclass variance, ensuring precise separation of brain structures from surrounding nonbrain tissues [32]. Morphological operations were subsequently applied to eliminate small isolated artifacts while preserving the largest connected component, corresponding to the brain region. The resulting mask was applied to the enhanced image, achieving a clean and accurate extraction of brain tissue.

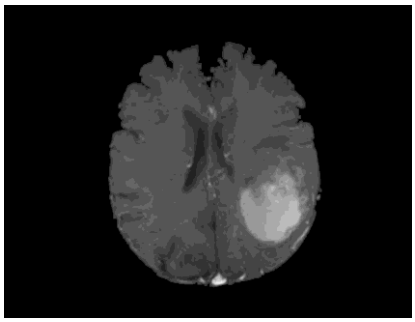

Fig. 5. Skull stripping of MRI image.

B. Gradient Calculation

To enhance edge detection within the image, we computed the gradient by taking the partial derivatives of the image intensity in the x and y directions [12, 33]. These derivatives, denoted as (M_x) and (M_y) represent the rate of change in intensity along each axis. Subsequently, these gradients were combined to produce the gradient magnitude, which quantifies intensity variations across the image and aids in detecting boundary transitions (Fig. 6). The gradient magnitude was computed using a standard formula, designed to capture even subtle intensity variations, thereby providing a more precise representation of image edges:

$$h = (|M_x|^3 + |M_y|^3)^{\frac{1}{3}} \quad (7)$$

This methodology effectively amplifies major intensity variations while reducing the impact of minor fluctuations. The resulting gradient magnitude map serves as a key tool for delineating image contours and boundaries, providing a solid foundation for subsequent segmentation and analysis. By accentuating regions of rapid intensity change, it ensures that prominent features are preserved, thereby facilitating more accurate and reliable brain tumor segmentation.

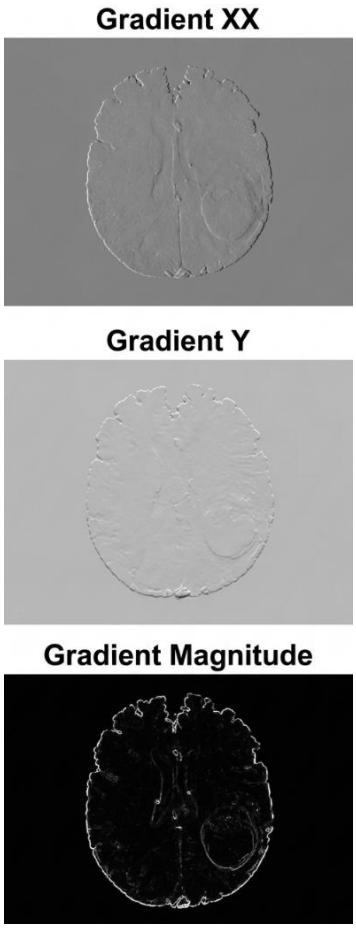

Fig. 6. Gradient calculation results.

C. Generating a Mask

To construct the initial segmentation mask, two unsupervised thresholding techniques were used: Kapur's entropy-based method and Otsu's variance minimization approach [34, 35]. These methods were selected for their distinct optimization criteria, the maximization of class information entropy and the minimization of intraclass variance which together provide complementary advantages for accurately delineating anatomical structures.

1) Kapur's entropy-based

Thresholding Kapur's entropy-based thresholding method (Fig. 7) seeks the optimal threshold T that divides the image histogram into two classes: foreground and background, such that the total entropy H, computed as the

sum of the entropies of both classes, is maximized. This measure reflects the amount of information and the separability of the segmented regions. That divides the image histogram into two classes: foreground and background. The entropy H for each threshold T is calculated as follows:

$$H(T) = -\left[\sum_{i=0}^{T} p(i)\log\left(p(i)\right) + \sum_{i=T+1}^{L-1} p(i)\log\left(p(i)\right)\right] \quad (8)$$

where *p(i)* is the probability of occurrence of gray level *i* and *L* is the total number of gray levels. The optimal threshold *T3* is the one that maximizes *H(T)*.

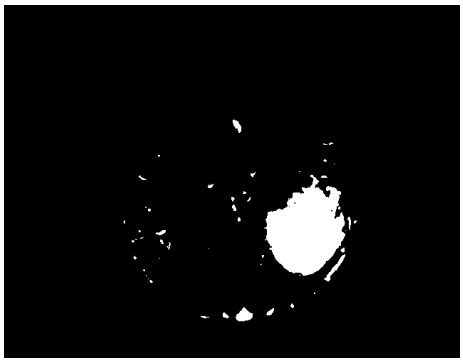

Fig. 7. Kapur thresholding.

2) Otsu's method

In the context of image segmentation, Otsu's method (Fig. 8) is used to identify an optimal threshold T that maximizes the variance between classes. This thresholding technique separates the image pixels into two distinct classes, typically foreground and background [36, 37]. The central objective is to minimize the within-class variance ($\sigma_w{}^2$), which is defined as the weighted sum of the variances of the foreground and background pixel distributions. Specifically, the within-class variance is given by:

$$\sigma_w{}^2 = w_1(T)\sigma_1{}^2(T) + w_2(T)\sigma_2{}^2(T) \quad (9)$$

where $w_1(T)$ and $w_2(T)$ are the weights of the classes (the proportions of pixels in each class) and $\sigma_1{}^2(T)$ and $\sigma_2{}^2(T)$ are the variances of each class. The optimal threshold T is the one that minimizes $\sigma_w{}^2(T)$.

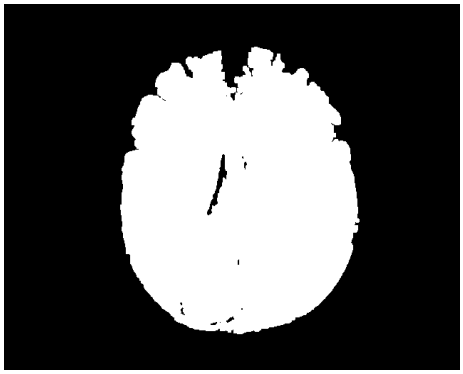

Fig. 8. Otsu thresholding.

To further refine the segmentation, the binary results (Fig. 9) obtained from the Kapur entropy-based method and the Otsu method were merged to generate a preliminary mask [38]. In this fusion process, pixels with a value of 2 in both methods' outputs were selected to form the final mask. This combined approach effectively leverages the strengths of both thresholding techniques, ensuring that the most reliable regions are preserved, which is critical for establishing a robust region of interest. The resulting mask serves as a strong foundation for the subsequent image processing stages, including advanced segmentation and feature extraction, where precision is paramount.

Fig. 9. Final mask.

D. Point and Mask Generation

To generate and rigorously evaluate quasi-random point sequences for brain tumor segmentation, a diverse set of sampling methods was employed, including the Halton, Sobol, Hammersley, Faure, and Poisson Disk Sampling techniques [39, 40]. Initially, the Halton sequence was used. It leverages prime bases for each dimension, producing a quasi-random distribution with reduced correlation in lower dimensional spaces. This approach is particularly useful for lower-dimensional feature spaces, as it ensures effective point dispersion with limited interdimensional dependency [30]. Building on this foundation, the Sobol sequence was applied, renowned for its low-discrepancy properties, which guarantee a highly uniform distribution of points even in high dimensional spaces. This feature is critical for multidimensional datasets, as it ensures that the sampling process captures essential image features without excessive concentration or clustering [41]. The Hammersley sequence was also tested. It combines sequence numbers with Halton sequences, enhancing the uniformity and efficiency of point distribution in lower-dimensional contexts [32]. This sequence is particularly effective in scenarios where the dimensionality is not excessively high, thus ensuring optimal space coverage with minimal overlap. To address higher-dimensional challenges, the Faure sequence was adopted. It extends Halton's method by introducing digit permutations, resulting in improved uniformity in higher-dimensional spaces. This refinement is valuable for complex imaging tasks, where maintaining uniformity across multiple dimensions is essential. Finally, Poisson Disk Sampling was incorporated, generating points that

maintain a minimum distance from one another, thereby reducing clustering and ensuring a more uniform spatial distribution. This property is critical for segmentation applications, as it minimizes overlapping or redundant points and supports more accurate delineation of tumor and edema boundaries [42]. The resulting point sets underwent both qualitative and quantitative assessments to evaluate their ability to efficiently fill the image space. A comparative analysis was conducted to assess performance in terms of uniformity and spatial coverage. The points generated through these quasi-random sequences were then integrated into the image processing pipeline to analyze their impact on segmentation accuracy, particularly for brain tumor detection in MRI images. The comprehensive evaluation of these methods combining visual inspection and computational metrics, provided key insights into their effectiveness in improving segmentation robustness and precision, forming the basis for subsequent image analysis steps [43].

To achieve precise segmentation, the Expectation Maximization (EM) algorithm was used to divide the subset of points into k classes C_i (where $i = 1, ..., k$). This clustering method assigns the points into different classes based on their frequencies and intensities. Each class is characterized by a parameter vector θ_i (m_i and σ_i), where m_i is the mean and σ_i is the variance of C_i (for $i = 1, ... ,k$) [44]. The EM algorithm refines these parameters using the following log-likelihood function:

$$lnPr(lik|p,c|\theta,\pi_i = \sum_{j=1}^{1} ln(\sum_{1=1}^{k} \pi_i N(p_j|\theta_i)) \quad (10)$$

where

$$N(p_j|\theta_i) = \frac{1}{\sqrt{2\pi\sigma_i^2}} exp\left(-\frac{(p_j - m_i)^2}{2\sigma_i^2}\right) \quad (11)$$

where, π_i denotes the mixing coefficient, and $\sum_{i=1}^{k} \pi_i = 1$ The EM algorithm iterates to refine the estimates. It stops when the change in the parameter estimates falls below a predefined threshold ε and when the log-likelihood stabilizes over a width convergence window of width w. The convergence of the EM algorithm is visually represented in Fig. 3, showing the variation of log-likelihood probability with the number of iterations, where the red line indicating the convergence limit.

Following clustering, segmentation was initialized using seed points derived from the clusters [32]. Each seed point P_{seedi} was selected based on its proximity to the mean intensity mi satisfying the following condition:

$$|I(P_{seedi}) - m_i| \leq \min_{1<j<l} |(I(P_j) - m_i| \quad (12)$$

This ensures that the initial seeds are well-positioned to accurately define the Regions of Interest (ROI) [43]. From these seed points, the segmentation was extended using a region-growing technique, which progressively refined the final segmentation outcome.

E. Segmentation

After selecting the initial seed points, the segmentation for each class is executed using a modified region-growing technique. A key drawback of the traditional region-growing method is its dependence on accurate seed selection and the definition of homogeneity criteria. In the classical approach, the region expands by incorporating neighboring pixels based on a similarity measure. However, if the initial seed lies in a heterogeneous region, the similarity measure may yield inconsistent or abnormally high values, leading to premature termination of region growth. Consequently, selecting seeds from homogeneous regions becomes essential [45, 46]. Moreover, inadequate or overly strict homogeneity thresholds can result in under- or over-segmentation of the ROI [12, 47]. To mitigate these issues, the segmentation process is initiated using an initiator Pseedi for each class. The homogeneity criterion is set to $2 \times \sigma_i$, while the class mean is denoted by m_i. In addition, to preserve the integrity of segmented boundaries, gradient magnitude information is utilized to prevent overlap and ensure clearer separation between adjacent regions [43, 48]. The subsequent algorithm details the multi-region growing segmentation process.

Algorithm: Multi-Region Growing Segmentation

Inputs:
- $I(x,y)$: input image
- P_{seedi}: initiator seed of class i
- C_i: set of pixels allowed for class i
- Δint: minimum intensity distance
- $\Delta gradient$: minimum gradient intensity distance
- m_i: initial mean of class i
- Gm_i: average gradient of class i

Output:
- R_i: region i

Begin
1. Initialize the region R_i with pixels assigned to the class.
2. Repeat
(a) $V(P_{seedi})$ = neighborhood of P_{seedi}
(b) borderlist = borderlist$\cup V(P_{seedi})$
(c) Order borderlist by Δint
(d) P_{seedi}= the first pixel in borderlist that satisfies
- $|I(P) - m_i| < \Delta int$ and
- $|\text{Gradient}(P) - Gm_i| < \Delta gradient$

(e) **If** P_{seedi} exists **Then**
i. $R_i = R_i \cup P_{seedi}$
ii. borderlist = borderlist $\backslash P_{seedi}$
iii. Update m_i
(f) **Else**
i. Break
3. Until P_{seedi} no longer exists

F. Performance Evaluation

To rigorously evaluate the performance of brain tumor segmentation, a comprehensive set of evaluation metrics was used to ensure both accuracy and robustness in the assessment. The Dice coefficient, also known as the Sørensen-Dice index, serves as a key metric for measuring the agreement between the predicted segmentation and ground-truth reference. This metric is mathematically defined as:

$$\text{Dice Coefficient} = \frac{2\times|X\cap Y|}{|X|+|Y|} \quad (13)$$

where X is the predicted segmentation and Y is the ground truth, with a value of 1 indicating a perfect match [49]. Sensitivity, often referred to as recall, measures the algorithm's proficiency in correctly identifying true positive pixels. It is expressed as:

$$\text{Sensitivity} = \frac{TP}{TP+TN} \quad (14)$$

where TP is the number of true positives and FN is the number of false negatives [50]. Specificity, a critical metric in assessing the accuracy of the segmentation algorithm's identification of negative pixels, is quantified as:

$$\text{Specificity} = \frac{TN}{TN+FP} \quad (15)$$

with TN representing true negatives and FP representing false positives [50]. In conjunction with the aforementioned metrics, the Hausdorff Distance (HD) is employed to rigorously evaluate the geometric correspondence between the predicted and ground truth segmentations, particularly for tumor and edema delineation. This metric quantifies the maximum spatial deviation between the contour points of the two segmentations and is formally defined as:

$$HD = \max(sup_{x\epsilon X} inf_{y\epsilon Y} d(x,y), sup_{x\epsilon Y} inf_{y\epsilon X} d(x,y) \quad (16)$$

where $d(x,y)$ is the Euclidean distance between points x and y [32]. For both tumor and edema regions, the Hausdorff distance serves as a critical tool for detecting substantial localization errors, including missed detections and misplaced regions. This measure highlights the most significant discrepancies in boundary placement, providing a comprehensive evaluation of segmentation accuracy. Finally, the Average Distance (AVD) metric is utilized to compute the mean distances between each point in the predicted segmentation and its corresponding nearest point in the ground truth. This metric is defined as:

$$\text{Average Distance} = \frac{1}{|X|}\sum_{x\epsilon X} min_{y\epsilon Y} d(x,y) \quad (17)$$

where $|X|$ is the number of points in the predicted segmentation [32]. The combination of these metrics offers a robust and comprehensive framework for evaluating segmentation performance, taking into account both global and local alignment between predicted segmentation and ground truth, specifically for tumor and edema regions. Considering both the overall accuracy and the finer details of the segmentation boundaries, these metrics facilitate a more nuanced understanding of the algorithm's performance. Furthermore, they enable a detailed comparative analysis of the five quasi-random point sequences. Halton, Sobol, Hammersley, Faure, and Poisson Disk, thus providing valuable insight into the relative efficacy of each sequence in the context of segmentation tasks [43].

IV. Results and Discussion

This section presents an in-depth evaluation of the results of brain MRI segmentation obtained through the integration of five quasi-random point sequences—Halton, Hammersley, Sobol, Faure, and Poisson Disk—within both a region-growing framework and an Expectation-Maximization (EM)- based segmentation approach. Each sequence was used to guide the spatial sampling process, thereby influencing the evolution of the segmented regions in the case of region-growing, and serving as an initialization strategy for parameter estimation in the EM framework. To rigorously assess the performance of these approaches, a comprehensive suite of quantitative metrics was used, including the Dice similarity coefficient, Sensitivity, Specificity, Hausdorff Distance (HD), and Average Distance (AVD). These indicators provide a multifaceted evaluation of segmentation quality, in terms of spatial accuracy, boundary delineation, and detection sensitivity. The results are systematically analyzed and compared across multiple case studies to discern the most effective sequence-method combination for precise identification of tumoral and edematous structures in brain MRI images.

A. Description of the Images Used

In this investigation, three high-resolution Magnetic Resonance Imaging (MRI) scans (Fig. 10), each exhibiting a distinct pathological manifestation of brain neoplasms, were carefully selected to serve as benchmark data for the empirical validation of the segmentation framework. Each image is accompanied by expertly curated ground truth annotations, delineating with precision the spatial extent of both tumoral and peritumoral (edematous) regions. These expert-labeled references, derived from clinically validated diagnostic interpretations, constitute an indispensable standard for objectively assessing segmentation accuracy. The incorporation of such authoritative ground truth data confers a high degree of methodological rigor, enabling reproducible and objective quantification of segmentation performance. This evaluation process is applied to the region-growing paradigm, systematically combined with a suite of quasi-random point sampling strategies—Halton, Hammersley, Sobol, Faure, and Poisson Disk, each selected for its theoretical strengths in exploring the spatial domain. The availability of precise reference delineations not only enhances the statistical reliability of comparative analyses, but also ensures robust validation of the proposed methodological framework within the broader context of medical image segmentation.

B. Results for Each Image

To evaluate the segmentation performance of the five quasi-random sampling methods on three MRI datasets, we employed a set of standard and complementary quantitative metrics. The Dice Similarity Coefficient was used to assess the volumetric overlap between the

predicted segmentation and the ground truth, while sensitivity measured the ability to correctly identify lesion voxels (true positives), and specificity quantified the accuracy in identifying non-lesion tissue (true negatives). The Hausdorff Distance (HD) captured the maximum boundary deviation, thereby reflecting the worst-case geometric error, while the Average Distance (AVD) provided a finer measure of the mean contour discrepancy. All metrics were computed separately for the tumor (R1) and edema (R2) regions, allowing a comprehensive analysis of both core and peripheral lesion segmentation quality.

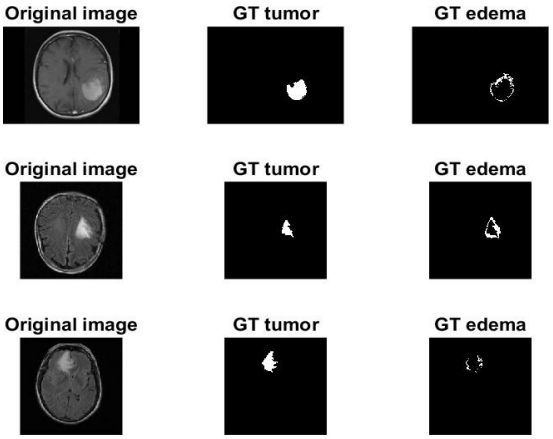

Fig. 10. Original image with ground truth Images of tumor and edema.

For Image 01 (Fig. 11) with the results reported in Table I, the Hammersley sequence exhibited exceptional performance in terms of the Dice coefficient, reaching 97.87% for region R1, reflecting a highly accurate volumetric segmentation. This sequence also demonstrated a sensitivity of 95.66%, indicating strong tumor detection capability. The notably low Average Distance (AVD) of 0.10 further indicated optimal segmentation boundary precision. In contrast, the Sobol sequence, though slightly below Hammersley in terms of Dice (95.29%), still showed strong results with a high sensitivity of 95.71% and stable values of Hausdorff Distance (HD) and AVD (11.18 and 0.29, respectively). This suggests that while Sobol offers slightly lower volumetric accuracy, it maintains robust detection performance with consistent results across images. The Poisson sequence also performed competitively, particularly for region R2, with a Dice coefficient of 86.78% and an AVD of 0.45. Although these values are slightly higher than those of Sobol, they remain acceptable in terms of boundary precision. However, the Faure sequence showed a substantial degradation in performance for edema detection in region R2, with a very low Dice coefficient of 49.18% and a sensitivity of 32.12%. This degradation can be attributed to the insufficient coverage of poorly defined regions, such as the edema borders, a likely consequence of the irregular spatial distribution of the Faure sequence.

Fig. 11. Original image 01 with results obtained using the Sobol, Halton, Hammersley, Poisson, and Faure sequences, in order.

TABLE I. SEGMENTATION PERFORMANCE ON IMAGE 01 USING DIFFERENT SAMPLING SEQUENCES

Sequence	Dice (%)		Sensitivity (%)		Specificity (%)		HD		AVD	
	R1	R2	R1	R2	R1	R2	R1	R2	R1	R2
Sobol	95.29	94.81	95.71	96.04	99.90	99.96	11.18	09.00	0.29	0.31
Hammersley	97.87	70.25	95.66	96.13	99.89	99.66	10.90	09.32	0.10	0.95
Halton	94.19	60.51	89.03	96.19	99.74	99.96	10.81	09.43	0.34	1.20
Faure	93.09	49.18	95.94	32.12	99.90	99.45	11.35	08.24	0.35	0.45
Poisson	95.87	86.78	92.07	87.23	99.81	99.88	10.86	08.77	0.27	0.45

Fig. 12 depicts the ROC curves for tumor segmentation (Region 1) obtained using the different quasi-random sampling sequences. The Sobol sequence shows the steepest and most favorable curve, achieving a sensitivity above 0.95 with a minimal false positive rate below 0.001, confirming its excellent discriminative capability for tumor localization. The Hammersley and Faure sequences follow closely, both presenting smooth and rapidly rising curves that reach near-perfect sensitivity (TPR ≈ 0.99) for very small FPR values, highlighting their efficiency and reliability. The Poisson Disk sequence also exhibits well-balanced performance with a slightly gentler slope, suggesting slightly lower, yet still competitive detection accuracy. Conversely, the Halton sequence displays a slower sensitivity increase, indicating a modest trade-off between specificity and sensitivity compared to the other sequences. Overall, the ROC behavior indicates that the Sobol, Hammersley, and Faure sequences provide the most robust and precise classification performance for tumor segmentation, achieving high sensitivity while maintaining extremely low false positive rates.

Fig. 13 illustrates the ROC curves corresponding to edema segmentation (Region 2). The Sobol and Halton sequences exhibit almost identical and highly favorable trajectories, reaching sensitivity values above 0.96 with false positive rates below 0.001, thus confirming their exceptional discriminative power and consistency. The Poisson Disk and Hammersley sequences also perform strongly, showing smooth and steady sensitivity increases, reaching near-perfect detection levels (TPR > 0.98) for FPR values under 0.005. In contrast, the Faure sequence displays a markedly lower and delayed curve, with sensitivity values remaining limited for higher false positive rates, indicating reduced precision and weaker

ability to discriminate edema regions. Collectively, these results demonstrate that for edema segmentation, the Sobol and Halton sequences achieve the best trade-off between sensitivity and specificity, ensuring accurate and stable performance, while the Faure sequence remains the least effective among the tested quasi-random approaches.

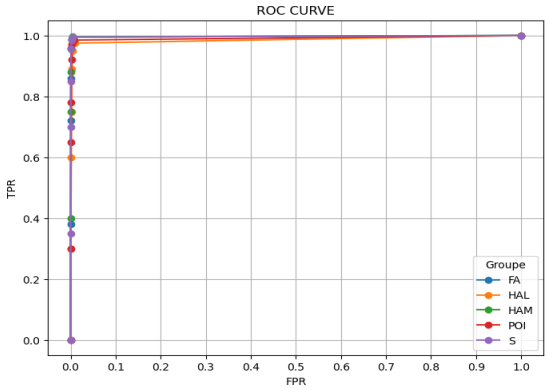

Fig. 12. ROC curves for the R1 region (tumor) of Image 01, comparing the performance of quasi-random sequences: S (Sobol), FA (Faure), HAL (Halton), HAM (Hammersley), and POI (Poisson).

For Image 02 (Fig. 14) with the results reported in Table II, the Sobol sequence once again proved superior, particularly in edema detection for region R2, with an outstanding Dice coefficient of 96.49% and a sensitivity of 97.74%. The Poisson sequence also achieved impressive results for the detection of edema (Dice = 92.67%), but was slightly weaker than Sobol in terms of sensitivity and Hausdorff distance (4.79 vs. 4.69), suggesting Sobol's better contour-tracking precision. Both Hammersley and Halton sequences recorded relatively weaker results in region R1, with Dice scores of 65.71% and 70.05%, respectively, indicating less accurate tumor segmentation. This observation underscores the tendency of these sequences to insufficiently focus on denser image regions, which are critical for precise tumor detection. The Faure sequence continued to show suboptimal results, with a low Dice coefficient in R1 (72.01%) and a sensitivity of 56.26%, indicating a poor capability to capture the essential features of the image. The relatively high AVD (0.45) reinforces this limitation, suggesting an inability to align the boundaries optimally.

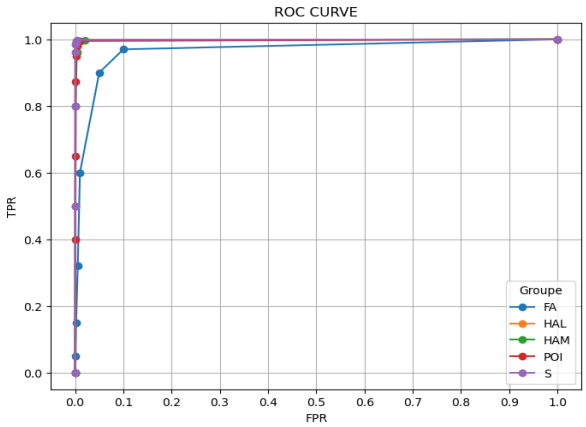

Fig. 13. ROC curves for the R2 region (edema) of Image 01, comparing the performance of quasi-random sequences: S (Sobol), FA (Faure), HAL (Halton), HAM (Hammersley), and POI (Poisson).

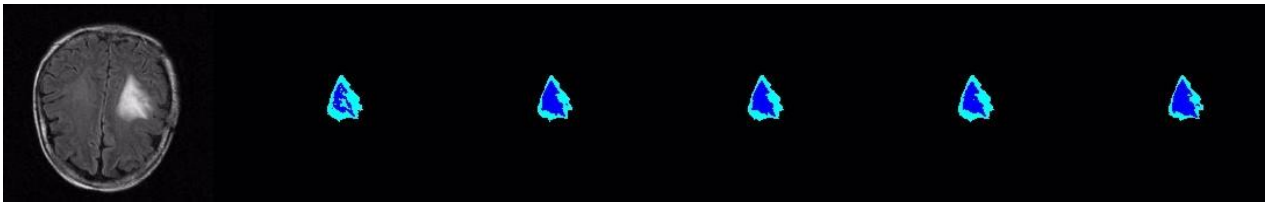

Fig. 14. Original image 02 with results obtained using the Sobol, Halton, Hammersley, Poisson, and Faure sequences, in order.

TABLE II. SEGMENTATION PERFORMANCE ON IMAGE 02 USING DIFFERENT SAMPLING SEQUENCES

Sequence	Dice (%)		Sensitivity (%)		Specificity (%)		HD		AVD	
	R1	R2	R1	R2	R1	R2	R1	R2	R1	R2
Sobol	86.44	96.49	76.12	97.74	99.68	99.97	4.69	5.09	0.06	0.10
Hammersley	65.71	68.83	48.94	98.45	99.33	99.98	4.35	5.29	0.22	0.54
Halton	70.05	74.83	53.90	90.31	99.40	99.90	4.35	5.00	0.20	0.42
Faure	72.01	71.13	56.26	82.50	99.43	99.80	4.35	5.00	0.18	0.45
Poisson	80.36	92.67	74.47	92.70	99.66	99.90	4.79	5.09	0.23	0.17

Fig. 15 illustrates the ROC curves obtained for the tumor region (R1) using the different quasi-random sampling sequences. The Sobol sequence exhibits the most favorable curve, characterized by a steep increase in sensitivity with minimal false positive rates, indicating a strong discriminative ability to distinguish tumoral from non-tumoral pixels. The Poisson Disk sequence follows a similar pattern, maintaining high sensitivity values with slightly higher false positive rates, reflecting consistent and accurate detection performance. The Hammersley and Halton sequences show smoother slopes and less pronounced curvature, suggesting a moderate trade-off between sensitivity and specificity and a tendency to misclassify regions with irregular boundaries. The Faure sequence demonstrates the least favorable behavior, with a slower rise in sensitivity and higher false positive rates, consistent with its weaker quantitative segmentation performance. Overall, the ROC analysis confirms that the Sobol and Poisson sequences provide the most efficient balance between sensitivity and specificity for precise tumor segmentation.

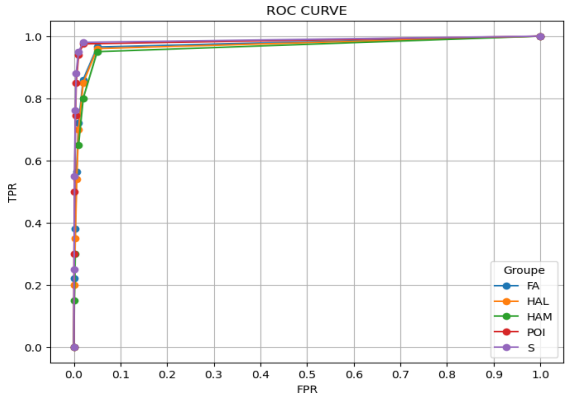

Fig. 15. ROC curves for the R1 region (tumor) of Image 02, comparing the performance of quasi-random sequences: S (Sobol), FA (Faure), HAL (Halton), HAM (Hammersley), and POI (Poisson).

Fig. 16 presents the ROC curves obtained for the edema region (R2) using the same quasi-random sequences. All methods reach high sensitivity and near-perfect specificity, reflecting the larger and more homogeneous structure of the edema compared to the tumor. Nevertheless, the Sobol sequence again produces the steepest and most optimal ROC curve, reaching almost perfect sensitivity ≈99% with an extremely low false positive rate ≈0.0003, demonstrating exceptional discriminative power. The Poisson Disk and Hammersley sequences also perform strongly, maintaining high sensitivity and stable detection across thresholds. The Halton and Faure sequences, however, show slower progression in sensitivity, indicating less accurate delineation of edema boundaries. These observations further validate the superior robustness of the Sobol sequence, followed by the Poisson sequence, in accurately identifying and segmenting edema regions with minimal classification error.

For Image 03 (Fig. 17) with the results reported in Table III, the Hammersley sequence again demonstrated remarkable results in region R1, achieving a Dice coefficient of 96.52% and a sensitivity of 93.28%, with a very low AVD of 0.06. This indicates a particularly precise and well-localized tumor segmentation. However, its performance in R2 was less impressive, which is a recurring behavior in this sequence, suggesting a tendency to under segment edema regions. The Sobol sequence, while slightly lower in R1 (Dice = 91.91%), showed strong consistency between regions, with relatively low HD and AVD values (5.00 and 0.14, respectively). The Faure sequence, which continued to underperform in R2 (Dice coefficient = 68.69%) and showed modest AVD values, once again demonstrated an inability to capture the contours of the target structures effectively. This limitation could be explained by intrinsic drawbacks in the point distribution method, where regularity is insufficient to ensure precise detection in complex regions such as edema.

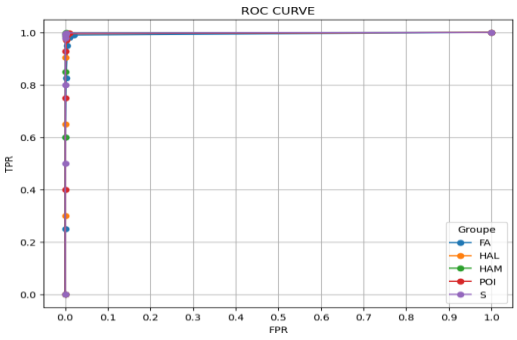

Fig. 16. ROC curves for the R2 region (edema) of Image 02, comparing the performance of quasi-random sequences: S (Sobol), FA (Faure), HAL (Halton), HAM (Hammersley), and POI (Poisson).

Fig. 17. Original image 03 with results obtained using the Sobol, Halton, Hammersley, Poisson, and Faure sequences, in order.

TABLE III. SEGMENTATION PERFORMANCE ON IMAGE 03 USING DIFFERENT SAMPLING SEQUENCES

Sequence	Dice (%)		Sensitivity (%)		Specificity (%)		HD		AVD	
	R1	R2	R1	R2	R1	R2	R1	R2	R1	R2
Sobol	91.91	83.11	85.03	81.00	99.74	99.92	5.00	5.00	0.14	0.12
Hammersley	96.52	76.50	93.28	73.46	99.88	99.89	5.00	5.00	0.06	0.13
Halton	85.87	65.32	75.24	97.80	99.57	99.99	5.00	5.00	0.18	0.31
Faure	75.36	68.69	60.46	90.85	99.32	99.95	5.00	5.00	0.19	0.28
Poisson	88.20	80.00	78.89	79.14	99.64	99.91	5.00	5.00	0.17	0.14

Fig. 18 presents the ROC curves corresponding to tumor segmentation (Region 1) using the different quasi-random sequences. The Sobol sequence exhibits the most favorable trajectory, achieving rapid growth in sensitivity with almost negligible false positive rates (FPR < 0.005), which highlights its remarkable discriminative capacity for tumor detection. The Poisson sequence shows a similar but slightly less steep progression, maintaining a balanced trade-off between sensitivity and specificity and reaching near-perfect detection at high thresholds. The Hammersley sequence follows with a moderately smooth slope, denoting efficient yet slightly delayed sensitivity increase. In contrast, the Halton and Faure sequences display more gradual curves, reflecting slower sensitivity responses and higher false positive rates, consistent with their lower quantitative segmentation performance. Overall, the ROC curves for tumor segmentation confirm that the Sobol and

Poisson sequences achieve the highest classification accuracy, ensuring robust and reliable identification of tumoral regions.

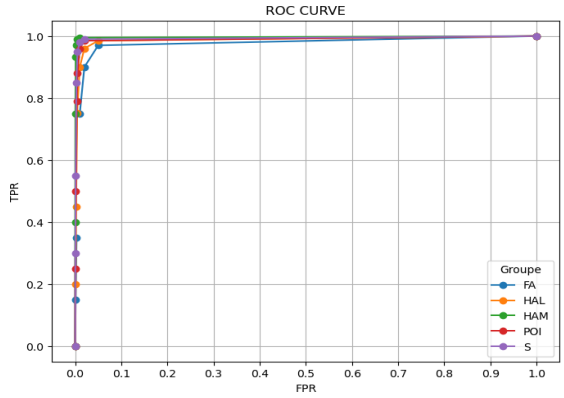

Fig. 18. ROC curves for the R1 region (tumor) of Image 03, comparing the performance of quasi-random sequences: S (Sobol), FA (Faure), HAL (Halton), HAM (Hammersley), and POI (Poisson).

Fig. 19 illustrates the ROC curves obtained for edema segmentation (Region 2). The Halton sequence clearly stands out, with an exceptionally steep curve that reaches high sensitivity values (TPR > 0.97) even for minimal false positive rates (FPR < 0.001), indicating superior stability and precision in edema detection. The Faure and Sobol sequences also perform well, showing consistent increases in sensitivity while maintaining low error rates. The Poisson and Hammersley sequences, though following comparable patterns, present slightly flatter slopes, suggesting a more gradual separation between positive and negative cases. These results demonstrate that for edema segmentation, the Halton sequence offers the most optimal balance between sensitivity and specificity, while Sobol and Faure maintain competitive yet slightly less dominant performances. The overall ROC behavior confirms that quasi-random sequences can effectively adapt to different tissue characteristics, with Halton being particularly efficient for edema delineation.

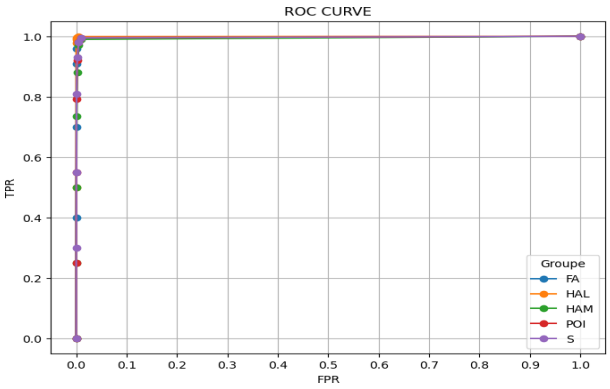

Fig. 19. ROC curves for the R2 region (edema) of Image 03, comparing the performance of quasi-random sequences: S (Sobol), FA (Faure), HAL (Halton), HAM (Hammersley), and POI (Poisson).

TABLE IV. AVERAGE SEGMENTATION PERFORMANCE ACROSS IMAGES USING DIFFERENT SAMPLING SEQUENCES

Sequence	Dice (%)		Sensitivity (%)		Specificity (%)		HD		AVD	
	R1	R2	R1	R2	R1	R2	R1	R2	R1	R2
Sobol	91.21	91.14	84.62	91.82	99.77	99.95	7.29	6.93	0.17	0.20
Hammersley	84.27	71.53	75.45	85.77	99.57	99.84	6.23	6.16	0.21	0.50
Halton	80.57	66.55	72.72	91.43	99.57	99.95	6.05	6.14	0.24	0.31
Faure	80.15	62.13	76.10	68.82	99.33	99.76	6.16	5.78	0.25	0.30
Poisson	81.56	79.48	73.47	85.14	99.65	99.90	6.22	5.97	0.21	0.24

For the average results across the images, Presented in Table IV, the Sobol sequence consistently delivered high quality results across all three images, showing a strong balance between volumetric accuracy and detection capability. On average, the Dice coefficient for the tumor region (R1) was 91.21%, while the edema region (R2) scored 91.14%. These values indicate robust segmentation of both tumor and edema areas, especially when compared to other sequences. Additionally, Sobol demonstrated excellent sensitivity values: 84.62% for R1 and 91.82% for R2, highlighting its ability to accurately identify true positive regions. The Hausdorff Distance (HD) values were 7.29 for R1 and 6.93 for R2, suggesting that Sobol excels in capturing regions, though boundary alignment can occasionally be slightly imprecise. In contrast, the Hammersley sequence showed notable strength in boundary precision, but slightly lower sensitivity compared to Sobol. On average, the Dice coefficient for R1 was 84.27% and 71.53% for R2, indicating excellent performance in dense tumor regions but underperformance in diffuse areas like edema. Sensitivity values were 75.45% for R1 and 85.77% for R2, while HD values were 6.23 for R1 and 6.16 for R2. Hammersley also achieved relatively low AVD values, averaging 0.21 for R1 and 0.50 for R2, confirming its accuracy in maintaining boundaries. The Poisson sequence demonstrated stable and reliable performance, although it was not the top performer. Dice coefficients averaged 81.56% for R1 and 79.48% for R2. Sensitivity scores were 73.47% for R1 and 85.14% for R2, indicating effective detection of most tumor and edema regions. HD values were 6.22 for R1 and 5.97 for R2, and AVD values were 0.21 for R1 and 0.24 for R2, showing slightly less precise boundaries than Sobol but generally robust performance for larger structures. The Faure sequence showed lower overall performance, with Dice coefficients of 80.15% for R1 and 62.13% for R2, and sensitivity values of 76.10% for R1 and 68.82% for R2. This highlights challenges in detecting true positive regions, particularly in diffuse areas like edema. HD values were 6.16 for R1 and 5.78 for R2, and AVD values were 0.25 for R1 and 0.30 for R2, emphasizing limitations in precise boundary alignment. Finally, the Halton sequence demonstrated moderate performance, with Dice coefficients of 80.57% for R1 and 66.55% for R2. Sensitivity scores were 72.72% for R1 and 91.43% for R2, and HD values were 6.05 for R1 and 6.14

for R2, with AVD values of 0.24 for R1 and 0.31 for R2. This indicates that Halton can capture general regions but may miss true positives and has moderate boundary precision. In conclusion, the Sobol sequence consistently outperformed the others, delivering superior segmentation quality with high volumetric accuracy and detection capability for both tumor and edema regions Hammersley also demonstrated excellent boundary precision, though its sensitivity in less defined areas was lower. Poisson exhibited stable and reliable results for larger regions, with minor boundary limitations. Faure and Halton sequences, while somewhat stable in certain areas, struggled to achieve high sensitivity and precise boundaries, limiting their applicability in tasks requiring high segmentation accuracy.

C. Results Interpretation

Comparative analysis of segmentation performance across the three MRI datasets, using five distinct quasi-random sampling sequences, reveals clear differences in the effectiveness of each method. These performance differentials highlight the impact of point distribution strategies on the accuracy and robustness of brain tumor delineation.

The Sobol sequence emerges as the preeminent method across all evaluated sequences, consistently achieving superior Dice Coefficient values and demonstrating exceptional sensitivity across the three MRI datasets. These results, as illustrated in Figs. 20 and 21, reflect Sobol's ability to maintain a high degree of congruence with the ground truth, effectively capturing true positives in tumor delineation. While it exhibits a slightly higher Hausdorff Distance and Average Distance compared to some other sequences, the Sobol sequence's remarkable balance between high overlap accuracy and sensitivity ensures its outstanding reliability for precise and robust brain tumor segmentation.

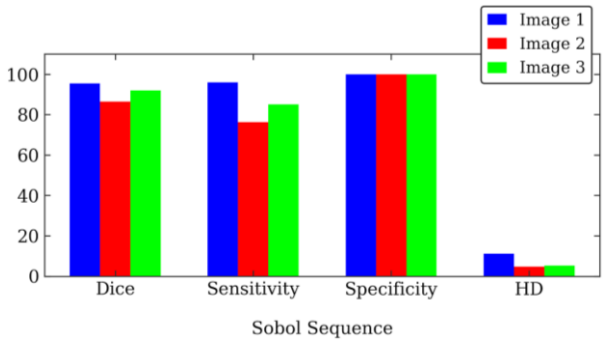

Fig. 20. Performance metrics for the Sobol sequence.

The Hammersley sequence demonstrates notable strengths, particularly in terms of Hausdorff Distance and specificity, indicating its aptitude for precise boundary localization and the reduction of false positives. As shown in Figs. 22 and 23, However, its comparatively lower Dice Coefficient values in certain cases reveal limitations in capturing the full extent of tumor regions. This discrepancy suggests that, although the Hammersley sequence is proficient in outlining lesion contours, it may be less effective in achieving comprehensive overlap with the ground truth. Nonetheless, its consistently high specificity, combined with commendable sensitivity, highlights its potential as a reliable method for conservative yet structurally accurate segmentation in brain tumor detection.

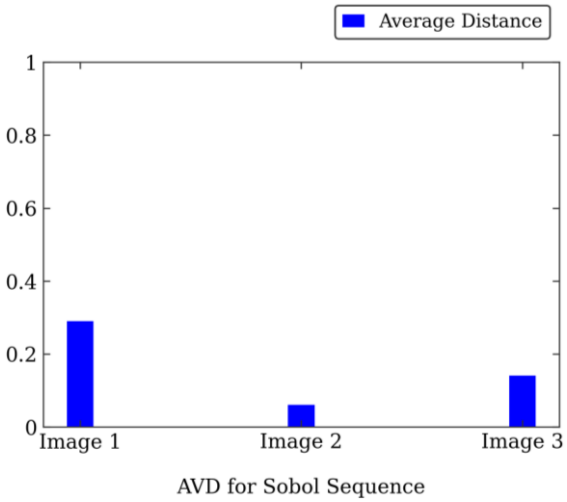

Fig. 21. Average Distance (AVD) for the Sobol sequence.

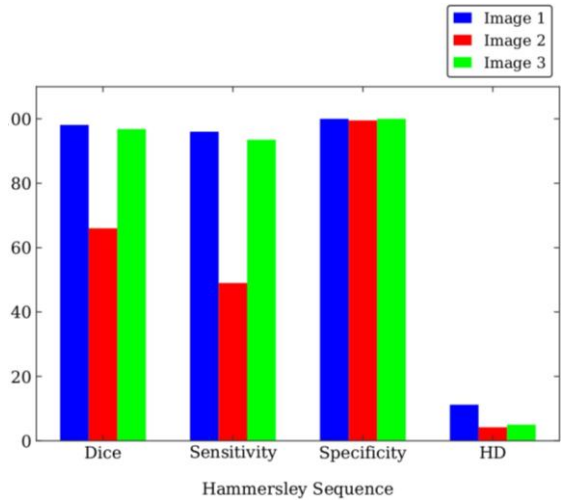

Fig. 22. Performance metrics for the Hammersley sequence.

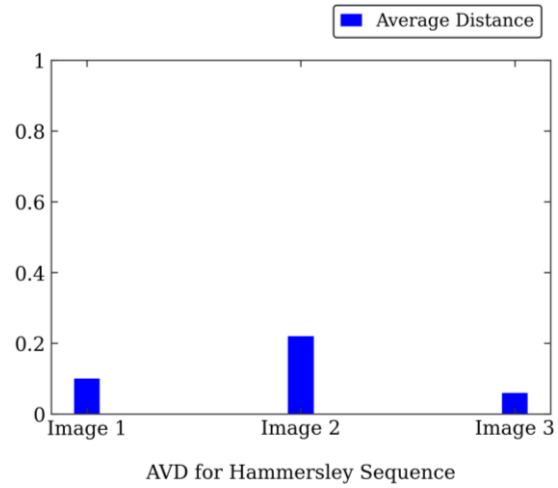

Fig. 23. Average Distance (AVD) for the Hammersley sequence.

The Poisson sequence demonstrated a commendably balanced performance, attaining solid results in terms of Dice Coefficient and Sensitivity, while preserving an adequate degree of boundary precision. Although it did not consistently dominate any single metric (as illustrated in Figs. 24 and 25), its ability to maintain stable and competitive outcomes across multiple evaluation criteria attests to its methodological robustness. This equilibrium between volumetric accuracy and contour delineation reflects the Poisson sequence's ability to deliver reliable and coherent segmentation, making it a viable and effective choice in scenarios demanding both general precision and structural fidelity.

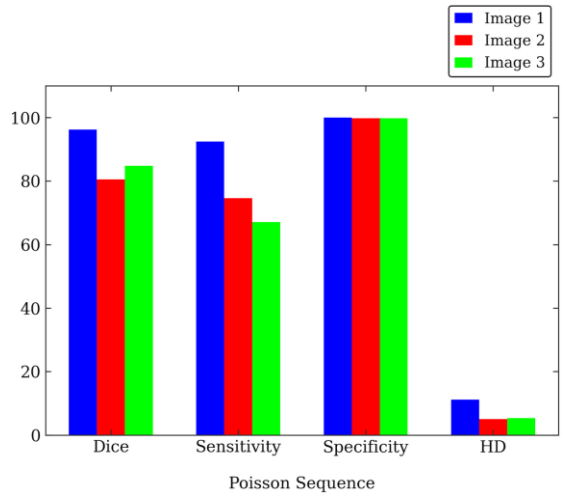

Fig. 24. Performance metrics for the Poisson sequence.

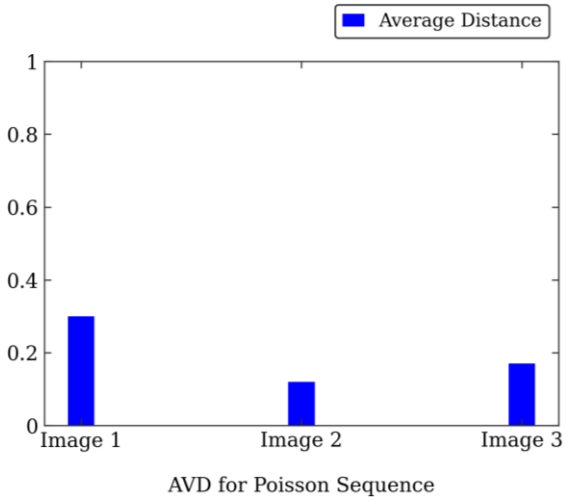

Fig. 25. Average Distance (AVD) for the Poisson sequence.

The Faure sequence consistently underperformed relative to the other quasi-random sampling methods, positioning it as the least effective within the comparative framework. As presented in Figs. 26 and 27, Its markedly lower Dice Coefficient and sensitivity values across the three images underscore substantial limitations in accurately capturing the extent of tumoral regions. The elevated Average Distance further reveals imprecise boundary delineation, suggesting a lack of spatial coherence in the segmentation output. While the method maintained commendable specificity—indicating an ability to avoid false positives—this isolated strength is insufficient to offset its broader deficiencies in segmentation completeness and anatomical accuracy. As such, the Faure sequence demonstrates limited reliability for robust brain tumor segmentation.

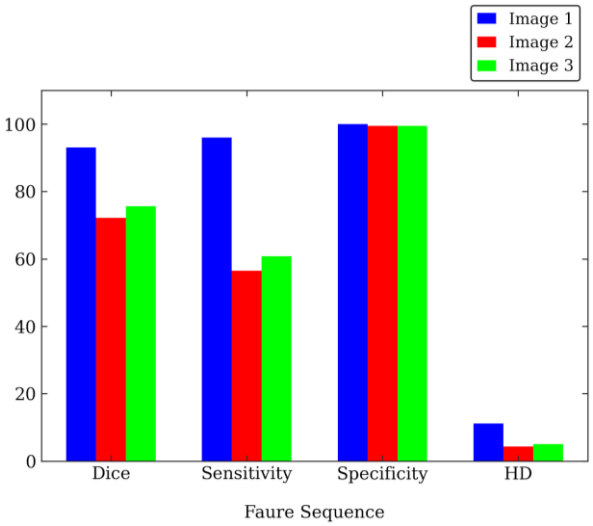

Fig. 26. Performance metrics for the Faure sequence.

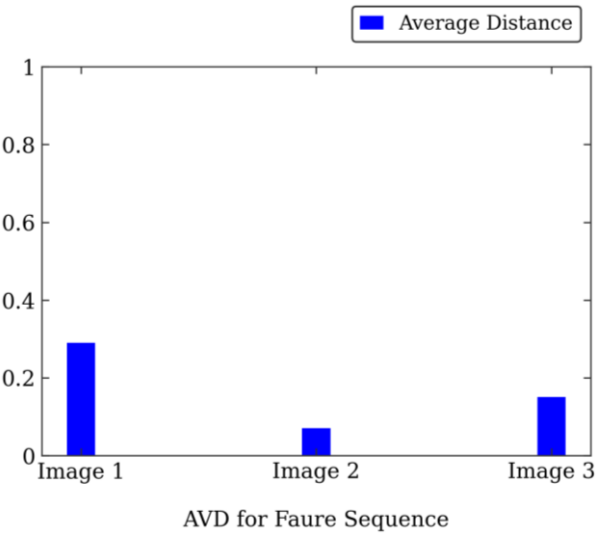

Fig. 27. Average Distance (AVD) for the Faure sequence.

The Halton sequence delivered an overall competitive performance, exhibiting solid Dice Coefficient values and satisfactory sensitivity across the evaluated images. As illustrated in Figs. 28 and 29, its comparatively higher Average Distance values indicate a relative weakness in boundary localization, particularly when contrasted with the more spatially precise Sobol and Hammersley sequences. This discrepancy suggests that while Halton is effective in identifying and segmenting tumor regions, it tends to yield less precise delineation of lesion contours. Consequently, its utility lies in robust detection, albeit with a moderate compromise in anatomical accuracy at the segmentation boundaries.

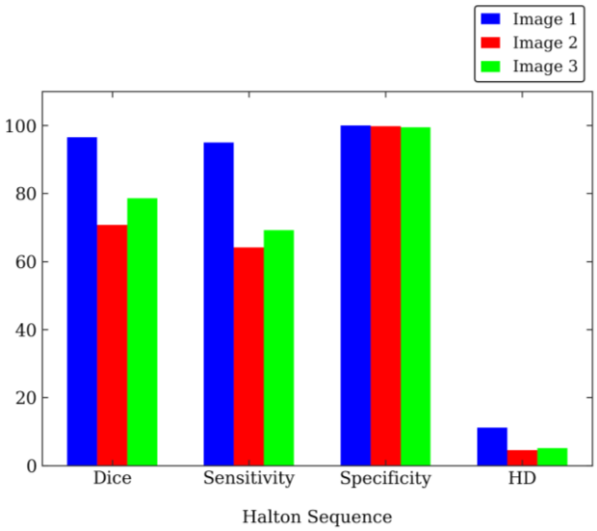

Fig. 28. Performance metrics for the Halton sequence.

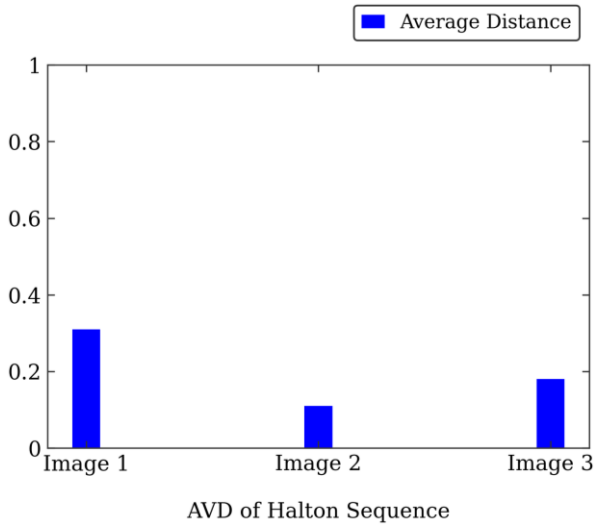

Fig. 29. Average Distance (AVD) for the Halton sequence.

While each quasi-random sequence has its specific strengths, the Sobol sequence stands out as the most balanced and reliable for brain tumor segmentation, delivering solid performance across most evaluation criteria. This superiority can be justified by analyzing the discrepancy, spatial uniformity, and sampling correlation properties of each quasi-random sequence. The Sobol sequence achieved the highest Dice and Sensitivity values due to its exceptionally low discrepancy and superior uniform coverage in multi-dimensional domains. These properties ensure that the sampled pixels used as inputs to the Expectation-Maximization (EM) and region-growing stages are statistically well-distributed and representative of the image intensity space. This leads to more accurate estimation of the Gaussian mixture parameters (μ_i, σ_i) and to more reliable seed selection, producing smoother and anatomically consistent tumor boundaries, as reflected in its low AVD and competitive HD values.

D. Comparison with Previous Reported Works

When compared to recent state-of-the-art studies on brain tumor segmentation (Table V), the proposed approach demonstrates highly competitive results across all quasi-random sampling strategies, with particularly strong performance achieved by the Sobol sequence. Previous studies have established important benchmarks: for instance, Zakariah *et al.* [51] reported one of the strongest recent results with a Dice coefficient of 85.45% and a Sensitivity of 94.49%, while Tejashwini *et al.* [52] achieved a Dice of 84.5% and a Hausdorff Distance (HD) of 8.1 mm. Other methods, such as that by Vossough *et al.* [53], reported lower metrics (Dice = 75%, HD = 12.3 mm). In direct comparison, the Sobol sequence in the present work sets a new performance benchmark. It achieved Dice scores of 91.21% (R1) and 91.14% (R2), significantly surpassing the best previously published result (Zakariah *et al.* [51], 85.45%). Although Zakariah *et al.* [51] reported slightly higher Sensitivity (94.49%), the Sobol sequence maintains a very high level (84.62%–91.82%) while offering exceptional Specificity (99.77%–99.95%) and achieving a superior overall balance. Moreover, its Hausdorff Distances (7.29 mm and 6.93 mm) are lower than most reported values, including Tejashwini *et al.* [52] (8.1 mm), indicating better spatial consistency in boundary delineation. The Hammersley (Dice up to 84.27%) and Poisson (Dice up to 81.56%) sequences also produced highly competitive results, comparable to or slightly better than those reported by Tejashwini [52] and Vossough [53]. While the Halton and Faure sequences yielded more modest Dice scores (around 80% and below), they still demonstrate the overall effectiveness of the quasi-random sampling approach. In summary, these findings confirm that integrating quasi-random sampling significantly enhances segmentation quality and positions the proposed method—particularly when using the Sobol sequence—among the most accurate and robust approaches in recent state-of-the-art studies on brain tumor detection.

TABLE V. PERFORMANCE METRICS OF RECENT METHODS FOR BRAIN TUMOR SEGMENTATION

Study	Dice Coefficient (%)	Sensitivity (%)	Specificity (%)	Hausdorff (mm)
Tejashwini *et al.* [52] (2023, SLCA-UNet)	84.5	84.5	99.9	8.1
Vossough *et al.* [53] (2024, nnU-Net vs. DeepMedic)	75	63	99.9	12.3
Zakariah *et al.* [51] (2024, Dual Vision Transformer-DSUNET)	85.45	94.49	99.98	5.45

V. CONCLUSION

This study conducted a rigorous comparison of quasi-random sampling methodologies—namely, the Halton, Sobol, Hammersley, Faure, and Poisson Disk sequences—in the context of brain tumor segmentation in Magnetic Resonance Imaging (MRI). These low-discrepancy point distributions were embedded into a

multi-stage segmentation framework, combining Expectation-Maximization (EM) clustering with a refined region-growing algorithm. This approach led to substantial improvements in segmentation fidelity and boundary delineation accuracy. Among the sequences tested, the Sobol sequence consistently emerged as the most effective, achieving superior performance across multiple evaluation metrics, including the Dice Similarity Coefficient, Sensitivity, Specificity, Hausdorff Distance, and Average Distance (AVD). Its robustness is attributed to uniform spatial dispersion and low discrepancy, which improve seed point initialization and ensure anatomically consistent and reproducible segmentation. The Hammersley and Poisson Disk sequences also performed well, particularly in terms of boundary precision and specificity, but their results showed greater variability in region overlap accuracy. In contrast, the Faure and Halton sequences exhibited weaker performance, suggesting that their spatial sampling characteristics are less suited for capturing the complex morphological heterogeneity of gliomatous lesions. Overall, these findings highlight the importance of selecting appropriate sampling strategies to achieve reliable and consistent semi-automated medical image segmentation. The results strongly support the use of quasi-random sequences—especially Sobol—as a powerful tool for improving tumor segmentation in MRI. Future research will focus on optimizing Poisson-based sampling through adaptive parameterization and exploring hybrid quasi-random strategies to further enhance segmentation precision. Such developments could significantly advance high-fidelity medical image analysis, improving diagnostic accuracy and informing clinical decisions. A detailed comparison of the quasi-random sequences across performance metrics shows clear differences. The Sobol sequence achieved the highest Dice coefficient and sensitivity, indicating superior tumor detection and segmentation, and performed well in terms of Average Distance (AVD). The Hammersley sequence excelled in contour accuracy with the best Hausdorff Distance, though its Dice coefficient was more variable. The Poisson sequence offered a balance between Dice coefficient and contour precision. The Faure sequence generally underperformed in both tumor detection and boundary delineation. The Halton sequence, while promising, showed weaker contour accuracy compared to the top performers. In summary, the Sobol sequence is the most effective for brain tumor segmentation, while Hammersley and Poisson sequences also demonstrate notable performance. Future work will focus on optimizing the Poisson method and exploring hybrid or advanced quasi-random strategies to further improve segmentation accuracy and contour precision, potentially leading to better clinical outcomes.

Conflict of Interest

The authors declare no conflict of interest.

Author Contributions

B.S. (Corresponding Author) conceived and designed the study, developed the methodology, implemented the algorithms, and performed the experiments. He also wrote the original draft of the manuscript and is responsible for all communications with the journal. Z.C. and N.T. contributed to data curation and analysis, experimental validation, and the preparation of figures and tables. B.H. and E.B.B. provided crucial methodological guidance, supervised the project, and critically revised the manuscript for intellectual content. All authors reviewed and approved the final version of the manuscript.

References

[1] R. Kaifi, "A review of recent advances in brain tumor diagnosis based on ai-based classification," *Diagnostics*, vol. 13, 3007, 2023.

[2] C. Lekoui and A. Lahsasna, "Brain tumor detection using hybrid deep learning approaches," M.S. thesis, University of 20 August 1955—Skikda, 2024.

[3] M. Saranya and R. Praveena, "Accurate and real-time brain tumour detection and classification using optimized yolov5 architecture," *Scientific Reports*, vol. 15, 2025.

[4] R. Ranjbarzadeh, P. Zarbakhsh, A. Caputo, E. B. Tirkolaee, and M. Bendechache, "Brain tumor segmentation based on optimized convolutional neural network and improved chimp optimization algorithm," *Computers in Biology and Medicine*, vol. 166, 107723, 2023.

[5] A. Verma, S. N. Shivhare, S. P. Singh, N. Kumar, and A. Nayyar, "Comprehensive review on mri-based brain tumor segmentation: A comparative study from 2017 onwards," *Archives of Computational Methods in Engineering*, vol. 31, pp. 4805–4851, 2024. doi: 10.1007/s11831-024-10128-0

[6] M. Arbane, R. Benlamri, Y. Brik, and M. Djérioui, "Transfer learning for automatic brain tumor classification using MRI images," in *Proc. 2nd Int. Workshop Human-Centered Intell. Environ. Health Well-Being (IHSH)*, 2021, pp. 1–8. doi: 10.1109/IHSH51661.2021.9378739

[7] M. N. Islam, M. S. Azam, M. S. Islam, M. H. Kanchan, A. S. Parvez, and M. Islam, "An improved deep learning-based hybrid model with ensemble techniques for brain tumor detection from mri image," *Informatics in Medicine Unlocked*, vol. 47, 101483, 2024. doi: 10.1016/j.imu.2024.101483

[8] T. Shawly and A. Alsheikhy, "Classification of brain tumors using hybrid feature extraction based on modified deep learning techniques," *Computational Materials Continua*, vol. 76, no. 3, pp. 6435–6453, 2023. doi: 10.32604/cmc.2023.040561

[9] X. Wang and F. J. Hickernell, "Randomized Halton sequences," *Computers & Mathematics with Applications*, vol. 47, no. 10–11, pp. 1597–1616, 2004. doi: 10.1016/S0895-7177(00)00178-3

[10] M. R. Iacò, "Low discrepancy sequences: Theory and applications," arXiv preprint, arXiv:1502.04897, 2015.

[11] N. Kirk and C. Lemieux, "An improved halton sequence for implementation in quasi-monte carlo methods," arXiv Preprint, arXiv:2405.15799, 2024.

[12] N. A. Mohammed and S. S. Abdullah, "Impact of integral dimensions on halton and sobol sequences performance," *Journal of University of Duhok, Pure and Eng. Sciences*, vol. 22, no. 2, pp. 17–25, 2019. doi: 10.26682/sjuod.2019.22.1.3

[13] A. A. Jaoudé, *Recent Advances in Monte Carlo Methods*, IntechOpen, 2024. doi: 10.5772/intechopen.1000269

[14] N. Bonneel, D. Coeurjolly, J.-C. Iehl, and V. Ostromoukhov, "Sobol' sequences with guaranteed-quality 2D projections," *ACM Transactions on Graphics*, vol. 44, no. 4, pp. 1–16, 2025. doi: 10.1145/3730821

[15] E. Atanassov and S. Ivanovska, "On the use of sobol' sequence for high dimensional simulation," in *Proc. Computational Science—ICCS 2022*, London, UK, vol. 13297, 2022, pp. 646–652. doi: 10.1007/978-3-031-08760-8_53

[16] N. Dige and U. Diwekar, "Efficient sampling algorithm for large-scale optimization under uncertainty problems," *Computers & Chemical Engineering*, vol. 115, pp. 3–14, 2018. doi: 10.1016/j.compchemeng.2018.05.007

[17] T. Goda and K. Suzuki, "Recent advances in higher order quasi-monte carlo methods," arXiv Preprint, arXiv:1903.12353, 2019.

[18] A. B. Owen. (2023). Practical Quasi-Monte Carlo Integration. *Stanford University.* [Online]. Available: https://artowen.su.domains/mc/practicalqmc.pdf
[19] R. Kritzinger and F. Pillichshammer, "Exact order of extreme L_p discrepancy of infinite sequences in arbitrary dimension," *Arch. Math.*, vol. 118, pp. 169–179, 2022. doi: 10.1007/s00013-021-01688-9
[20] S. Tezuka, "Tractability of multivariate integration using low-discrepancy sequences," Kyushu University, Tech. Rep., 2016, pp. 23–43. doi: 10.1515/udt-2016-0013
[21] G. Leobacher and F. Pillichshammer, *Introduction to Quasi-Monte Carlo Integration and Applications*, 1st ed. Springer, 2014.
[22] J. Cheng and M. J. Druzdzel, "Computational investigation of low-discrepancy sequences in simulation algorithms for bayesian networks," in *Proc. Sixteenth Conf. Uncertainty in Artificial Intelligence (UAI 2000)*, Morgan Kaufmann, 2000, pp. 72–81.
[23] Y. D. T. O. V. Todorov and I. Dimov, "A comparison of quasi-monte carlo methods based on faure and sobol sequences for multidimensional integrals in air pollution modeling," *AIP Conference Proceedings*, vol. 2164, no. 1, 030002, 2019. doi: 10.1063/1.5130792
[24] O. Mogharrabi, B. Fathi, M. H. Behzadi, and R. Farnoosh, "The new scramble for Faure sequence based on irrational numbers," *Advances in Mathematical Physics*, vol. 2021, 6696895, 2021. doi: 10.1155/2021/6696895
[25] B. Vandewoestyne, H. Chi, and R. Cools, "Computational investigations of scrambled faure sequences," *Mathematics and Computers in Simulation*, vol. 81, no. 3, pp. 502–507, 2010. doi: 10.1016/j.matcom.2009.09.007
[26] N. Dwork, C. A. Baron, E. M. I. Johnson, D. O'Connor, J. M. Pauly, and P. E. Z. Larson, "Fast variable density Poisson-disc sample generation with directional variation for compressed sensing in MRI," *Magnetic Resonance Imaging*, vol. 74, pp. 152–162, 2021. doi: 10.1016/j.mri.2020.11.012
[27] C. Yuksel, "Sample elimination for generating Poisson disk sample sets," *Computer Graphics Forum*, vol. 34, no. 2, pp. 293–305, 2015. doi: 10.1111/cgf.12538
[28] Miccai brats database 2020. (2020). [Online]. Available: https://www.med.upenn.edu/cbica/brats2020/
[29] K.-N. Nguyen-Thi, H. Che-Ngoc, and A.-T. Pham-Chau, "An efficient image contrast enhancement method using sigmoid function and differential evolution," *Journal of Advanced Engineering and Computation*, vol. 4, no. 3, pp. 162–172, 2020. doi: 10.25073/jaec.202043.267
[30] P. Kalavathi and V. B. S. Prasath, "Methods on skull stripping of MRI head scan images—A review," *Journal of Digital Imaging*, vol. 29, pp. 365–379, 2016. doi: 10.1007/s10278-015-9847-8
[31] A. V. Lakshmi, V. Satyanarayana, and P. Mohanaiah, "Mri brain image enhancement using an improved contrast enhancement method," *Revista Gestão Inovação e Tecnologias*, vol. 11, no. 1, pp. 607–615, 2021.
[32] M. Laha, P. C. Tripathi, and S. Bag, "A skull stripping from brain MRI using adaptive iterative thresholding and mathematical morphology," in *Proc. 2018 4th International Conference on Recent Advances in Information Technology (RAIT)*, Dhanbad, India, 2018, pp. 1–6. doi: 10.1109/RAIT.2018.8389028
[33] H. Benjamin, K. Marc, B. Pablo, and E. Martin, "An approach toward fast gradient-based image segmentation," *IEEE Transactions on Image Processing*, vol. 24, no. 11, pp. 4503–4514, 2015. doi: 10.1109/TIP.2015.2419078
[34] S. Jardim, J. António, and C. Mora, "Image thresholding approaches for medical image segmentation—short literature review," *Procedia Computer Science*, vol. 226, pp. 181–188, 2023. doi: 10.1016/j.procs.2023.01.439
[35] Y. Jiang, D. Zhang, W. Zhu, and L. Wang, "Multi-level thresholding image segmentation based on improved slime mould algorithm and symmetric cross-entropy," *Entropy*, vol. 25, no. 1, 178, 2023. doi: 10.3390/e25010178
[36] Z. Jing and B. Tang, "Improved image segmentation method based on Otsu thresholding and level set techniques," *J. Phys.: Conf. Ser.*, vol. 2813, 012017, 2024. doi: 10.1088/1742-6596/2813/1/012017
[37] M. T. Nyo, F. Mebarek-Oudina, S. S. Hlaing *et al.*, "Otsu's thresholding technique for MRI image brain tumor segmentation," *Multimedia Tools and Applications*, vol. 81, pp. 43837–43849, 2022. doi: 10.1007/s11042-022-13215-1
[38] N. A. Ibrahim, E. R. Mohamed, H. M. Hamza, Y. S. Alsahafi, and K. M. Hosny, "Masked face image segmentation using a multilevel threshold with a hybrid fitness function," *Information Sciences and Applications (ISWA)*, 2024. doi: 10.1016/j.iswa.2024.200445
[39] A. Kumar, "Study and analysis of different segmentation methods for brain tumor MRI application," *Multimedia Tools and Applications*, vol. 82, no. 5, pp. 7117–7139, 2023. doi: 10.1007/s11042-022-13636-y
[40] W. H. Bangyal, K. Nisar, and A. A. B. A. Ibrahim, "Comparative analysis of low discrepancy sequence-based initialization approaches using population-based algorithms for solving the global optimization problems," *Applied Sciences (Switzerland)*, vol. 11, no. 16, 7591, 2021. doi: 10.3390/app11167591
[41] P. Praks and D. Brkić, "Approximate flow friction factor: Estimation of the accuracy using sobol's quasi-random sampling," *Axioms*, vol. 11, no. 1, 36, 2022. doi: /10.3390/axioms11020036
[42] T. B. Nguyen-Tat, T.-Q. T. Nguyen, H.-N. Nguyen, and V. M. Ngo, "Enhancing brain tumor segmentation in MRI images: A hybrid approach using UNet, attention mechanisms, and transformers," *Egyptian Informatics Journal*, vol. 27, 100528, 2024. doi: 10.1016/j.eij.2024.100528
[43] T. Speidel, J. Paul, S. Wundrak, and V. Rasche, "Quasi-random single-point imaging using low-discrepancy k-space sampling," *IEEE Trans. Med. Imaging*, vol. 37, no. 2, pp. 473–479, Feb. 2018. doi: 10.1109/TMI.2017.2760919
[44] A. A. Pravitasari, S. F. Qonita, and N. Iriawan *et al.*, "MRI-based brain tumor segmentation using gaussian and hybrid gaussian mixture model-spatially variant finite mixture model with expectation-maximization algorithm," *Malaysian Journal of Mathematical Sciences*, vol. 14, no. 1, pp. 77–93, 2020.
[45] J. Zhao, Z. Meng, L. Wei, C. Sun, Q. Zou, and R. Su, "Supervised brain tumor segmentation based on gradient and context-sensitive features," *Front. Neurosci.*, vol. 13, 144, 2019. doi: 10.3389/fnins.2019.00144
[46] E. S. Biratu, F. Schwenker, T. G. Debelee, S. R. Kebede, W. G. Negera, and H. T. Molla, "Enhanced region-growing for brain tumor MR image segmentation," *J. Imaging*, vol. 7, no. 2, 22, 2021. doi: 10.3390/jimaging7020022
[47] R. R. Mostafa, A. M. Khedr, Z. A. Aghbari, I. Afyouni, I. Kamel, and N. Ahmed, "Medical image segmentation approach based on hybrid adaptive differential evolution and crayfish optimizer," *Computers in Biology and Medicine*, vol. 180, 109011, 2024. doi: 10.1016/j.compbiomed.2024.109011
[48] Y. Gao, Z. Qi, and D. Zhao, "Edge-enhanced instance segmentation by grid regions of interest," *The Visual Computer*, vol. 39, no. 3, pp. 1137–1148, 2022. doi: 10.1007/s00371-021-02393-y
[49] Y. Xu, R. Quan, W. Xu, Y. Huang, X. Chen, and F. Liu, "Advances in medical image segmentation: A comprehensive review of traditional, deep learning and hybrid approaches," *Bioengineering*, vol. 11, no. 10, 1034, 2024. doi: 10.3390/bioengineering11101034
[50] T. Filleron, "Comparing sensitivity and specificity of medical imaging tests when verification bias is present: The concept of relative diagnostic accuracy," *Eur. J. Radiol.*, vol. 98, pp. 32–35, Jan. 2018. doi: 10.1016/j.ejrad.2017.10.022
[51] M. Zakariah, M. Al-Razgan, and T. Alfakih, "Dual vision Transformer-DSUNET with feature fusion for brain tumor segmentation," *Heliyon*, vol. 10, e37804, 2024. doi: 10.1016/j.heliyon.2024.e37804
[52] P. S. Tejashwini, J. Thriveni, and K. R. Venugopal, "A novel slca-unet architecture for automatic mri brain tumor segmentation," arXiv Preprint, arXiv:2307.08048, 2023.
[53] A. Vossough *et al.*, "Training and comparison of nnu-net and deepmedic methods for autosegmentation of pediatric brain tumors," *American Journal of Neuroradiology*, 2024. doi: 10.3174/ajnr.A8293